Model for Rotor Tip Vortex-Airframe Interaction, Part 1: Theory

H. Affes* and A. T. Conlisk†

Ohio State University, Columbus, Ohio 43210

The flowfield generated by a helicopter in flight is extremely complex, and it has been recognized that interactions among components can significantly affect helicopter performance. In the present work a simplified model for the interaction of a rotor tip vortex with the helicopter fuselage is developed. The tip vortex is idealized as a single three-dimensional vortex tube, and the fuselage is modeled as an infinite circular cylinder. The Biot-Savart law is employed to describe the flow induced by the vortex, and the flow is assumed to be inviscid and irrotational outside the core of the vortex. The numerical calculations indicate that a large adverse pressure gradient develops under the vortex on the fuselage causing a rapid drop in the pressure there; large variations in the curvature of the vortex are not observed. Numerical solutions for the vortex position and for the pressure on the airframe are calculated for the case where the vortex is embedded in a three-dimensional steady mean flow; the effect of vortex core size is also investigated. The nature of the initial stages of the breakdown of local axisymmetry of the core of the vortex filament is suggested based on both the numerical and experimental results.

Introduction

BECAUSE of increased maneuvering and load capacity requirements, recent work suggests that more information about the tip vortex-fuselage interaction is necessary to improve the design of the U.S. Army's helicopter fleet. Indeed, lack of understanding of the interaction between the tip vortex and solid surfaces has been identified as a major hurdle in predicting flows around complete rotorcraft configurations.[1] The focus of the present work is on a simplified model of such a tip vortex-fuselage interaction and consists of the analysis and computation of the motion of an infinitely long vortex tube passing above a circular cylinder. This vortex tube geometry is an idealization of the actual case where the tip vortex is a continuous helical tube of concentrated vorticity. The radius of curvature of the helix is approximately constant and very nearly the radius of the rotor[1]; if the fuselage or airframe radius is much less than the radius of the rotor, then as the filament approaches, it appears as a nearly straight filament oriented at approximately 90 deg to the generators of the cylinder. Thus the motion of a single vortex filament above the cylinder should be an adequate model for the actual physical situation during the period of interaction. In the present paper, the motion of the filament and its effect on the airframe before impact will be investigated in detail. The flow is assumed to be inviscid and irrotational outside the core of the vortex filament.

The motion of a three-dimensional vortex in free space has been documented by a number of authors, and excellent discussions of the previous work in this area is given by Hon and Walker[2] and Sarpkaya.[3] For the case where the vortex filament interacts with a body, the amount of work is much more limited and only simple body shapes such as a plane wall[2] and a sphere[4-7] have been considered; moreover, in general, the vortex filament shape is also restricted.[4-6]

In the rotorcraft area, Quakenbush and Bliss[8] have developed a "fat core" model based on the classical panel method designed to prevent the development of singularities when the vortex comes too close to the surface control panel points. Their objective is to reduce the large amplitude of the induced velocity as the vortex

collides with the surface by manipulation of the vortex core size, so that the numerical algorithm will not fail on collision. Komerath et al.[9] succeeded in modeling the periodic surface pressure fluctuations on the top of the airframe accurately using an existing rotor code that models the entire wake except during the time regime of significant vortex-surface interaction. Nominally, this time period runs from precollision through the postcollision phases. On the sides of the airframe, in the postcollision phase, they found large discrepancies between the computed surface pressure and the measured values. In fact, the pressure change is the opposite of what would be expected based on the superposition of a line vortex and singularities representing the airframe surface. The discrepancy was traced to the inability to predict the velocity field during significant vortex-surface interaction using a large-scale rotor wake code. This confirms the need for detailed analysis and computation of the vortex-surface interaction before further progress can be made in computing interacting flows around entire rotorcraft in the crucial operating regimes of hover and low-speed flight. Clearly, such an effort poses substantial challenges to both analytical approaches and to experiment, the latter because the phenomena in question occur on time scales on the order of 1 ms and involve highly three-dimensional flows. Moreover, the precise areas of deficiency in both experiment and theory do not become evident until detailed comparisons can be performed, proceeding systematically through the stages of the approach vortex trajectory and the precollision phenomena on the surface and then on to the impact and postcollision phases. In this paper we address, from a fundamental point of view, the characteristics of the approach vortex trajectory and the precollision phenomena on the surface as functions of vortex core size and mean flow speed.

Simons et al.[10] investigated the structure of the vortex filament shed from a rotor; they estimated the vortex core radius to be about 0.2 in. and noted that the core of the vortex may be turbulent. They also observed a rapid deformation of the vortex-core structure as the filament approached the supporting pylon of the rig. Liou et al.[11] have recently conducted experiments on the transient interaction between a cylinder and the vortex shed from a helicopter rotor (see also Brand et al.[12] and Brand[13]). They used laser Doppler velocimetry to measure the velocity in the vicinity of the filament and obtained results for the pressure on the surface of the cylinder under the impinging vortex. They were able to map the vortex position as a function of time, including the period during which a portion of the vortex impacts the cylinder. Bi and Leishman[14,15] and Leishman and Bi[16] also have reported on the interaction of the tip vortex with an airframe. The tip filament impinges on the aft part of the airframe in contrast to the work of Liou et al.,[11] and so
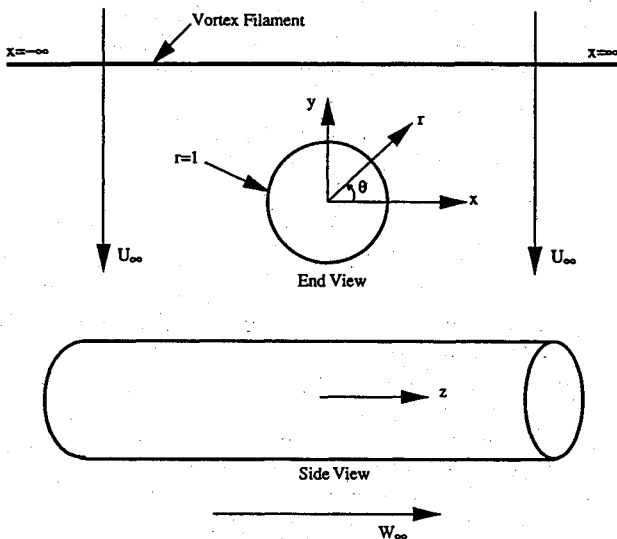
Fig. 1 Geometry of the present work; $r = 1$ denotes the cylinder surface.

the circulation of the filament is of the opposite sign. Both situations will be considered in the present work.

The experimental work just described indicates that the tip vortex will interact strongly with the airframe; recall that the vorticity field associated with the tip vortex is much stronger than that associated with the balance of the rotor wake, and so significant impulsive rotor loads may be generated. In the present work, a simplified model for this interaction is developed; in particular, the airframe is modeled as an infinite circular cylinder and the tip filament is taken to be straight and undeformed initially. The purpose of this paper is to present the theoretical tools to predict the vortex trajectory toward the cylindrical airframe and the pressure distribution on the cylinder under the vortex for a range of physical parameters and before the onset of strong interaction between the filament and the boundary layer on the airframe. The results indicate that, despite the relative simplicity of the model, many of the features of the vortex filament motion and the pressure field on the body seen in experiments[11-16] are reproduced. In this work, results are presented for a vortex in a three-dimensional streaming motion reminiscent of actual rotor flowfields. The effect of the vortex core size and the relative magnitude of the mean downwash and axial flow on the filament motion and the pressure distribution are also investigated. The effect of the image flowfield on the structure of the vortex as the filament approaches the cylinder is also considered.

This paper is the first of a two-part series on tip-vortex-airframe interaction. In Part 2,[17] the methods developed in this paper will be used to make quantitative comparisons with experiment. The plan of the paper is as follows. First, the problem is formulated, and the various elements in the calculation of the vortex filament motion are described in detail. In particular, the calculation of the image of the filament in the cylinder is performed using classical transform techniques. The numerical techniques employed to advance the filament in time and the calculation of the self-induced motion of the filament are detailed next. The results of the calculations are presented, and the paper concludes with a discussion of the genesis of the breakdown of the assumed vortex core structure as the vortex approaches the cylinder, followed by a summary and conclusions.

Formulation

We first consider the inviscid flow due to a generalized vortex filament of small cross section in a stagnant environment; the filament has strength Γ, and outside the filament the flow is assumed to be inviscid and irrotational. A typical initial vortex position is depicted in Fig. 1. The velocity potential due to the filament may be described by a velocity potential ϕ' that satisfies $\nabla^2 \phi' = 0$. Let

$\phi' = \phi_I + \phi_V$ where ϕ_V is the potential due to a vortex in free space. Then ϕ_I satisfies

$$\nabla^2 \phi_I = 0 \quad \text{with} \quad \frac{\partial \phi_I}{\partial r} = -\frac{\partial \phi_V}{\partial r} \quad \text{at} \quad r = 1 \quad (1)$$

and ϕ' must be bounded as $r^2 + z^2 \to \infty$. Here all lengths have been made dimensionless on the cylinder radius denoted by a, and ϕ' has been made dimensionless on $U_\infty a$ where U_∞ is a typical velocity. To simplify the calculations, we assume the cylinder is infinite in length. To obtain the solution to the boundary-value problem of Eq. (1), we use the Fourier transform in both the z and θ directions (Fig. 1); defining the double Fourier transform of ϕ_I as

$$\hat{\phi}_I = \int_{-\infty}^{\infty} \int_{-\pi}^{\pi} \phi_I \exp(-ikz - im\theta) \, d\theta \, dz \quad (2)$$

the transform solution $\hat{\phi}_I$ satisfies

$$\frac{\partial^2 \hat{\phi}_I}{\partial r^2} + \frac{1}{r} \frac{\partial \hat{\phi}_I}{\partial r} - \left(\frac{m^2}{r^2} + k^2\right)\hat{\phi}_I = 0 \quad (3)$$

Using the inversion formulas for the transforms as given in Churchill,[18] one may easily show that the velocity potential due to the presence of the cylinder, henceforth termed the image field, is given by

$$\phi_I = -\frac{1}{4\pi^2} \sum_{m=-\infty}^{\infty} e^{im\theta} \int_{-\infty}^{\infty} \frac{\partial \hat{\phi}_V}{\partial r}\bigg|_{r=1} \times \frac{K_m(|k|r)}{|k| K_m'(|k|)} e^{ikz} \, dk \quad (4)$$

where K_m is the modified Bessel function of order m. Note that $(\partial \phi_V / \partial r)|_{r=1}$ is the radial velocity at $r = 1$ due to a vortex filament in free space, which is defined by the Biot-Savart law; the transform in the z direction may be performed analytically, and after a significant amount of algebra, the transform of the radial velocity is given by[19]

$$\hat{U}_{Vr}\big|_{r=1} = \text{sgn}(\Gamma) \int_{-\pi}^{\pi} e^{-im\theta} \int_C [ikBK_0(c_1|k|)$$

$$+ A|k|K_1(c_1|k|)] e^{-ikz'} \, ds' \, d\theta \quad (5)$$

where

$$A = \frac{2}{c_1}[(\cos\theta - x')\sin\theta - (\sin\theta - y')\cos\theta] \frac{\partial z'}{\partial s'} \quad (6)$$

$$B = 2\left(\frac{\partial x'}{\partial s'}\sin\theta - \frac{\partial y'}{\partial s'}\cos\theta\right) \quad (7)$$

$$c_1 = \sqrt{(\cos\theta - x')^2 + (\sin\theta - y')^2} \quad (8)$$

and where, in Cartesian coordinates, the velocity field due to a vortex filament in free space is given by[20]

$$U_V(X, t) = -\text{sgn}(\Gamma) \int_C \frac{(X - X') \times dX'}{|X - X'|^3} \quad (9)$$

In Eqs. (6–8) the filament position is given by

$$X'(s', t) = x'(s')\hat{i} + y'(s')\hat{j} + z'(s')\hat{k}$$

where s' denotes a parametric variable defining the vortex filament. The C on the integral in Eq. (5) denotes integration over the space curve defining the vortex filament. The velocity potential given by Eq. (4) is expressed in polar coordinates; however, as will

be evident later, it is more convenient to advance the vortex filament in the Cartesian coordinate system defined in Fig. 1.

In a typical rotorcraft environment, the tip vortex is embedded in a downwash corresponding to the balance of the rotor wake superimposed on a velocity component along the airframe (forward flight). In the present work we model the effect of the balance of the rotor wake by a steady downwash corresponding to two-dimensional flow past a cylinder. In the coordinate system of Fig. 1 we have

$$U_M = \frac{\sin 2\theta}{r^2} \hat{i} - \left(1 + \frac{\cos 2\theta}{r^2}\right)\hat{j} + \alpha\hat{k} \qquad (10)$$

where $\alpha = W_\infty/U_\infty$ is the ratio of the mean velocity at infinity in the z direction to the characteristic velocity U_∞, which is the downwash mean velocity as $y \to \infty$. Note that the first two terms in Eq. (10) correspond to two-dimensional flow past a cylinder. For a vortex filament embedded in the mean flow given by Eq. (10) the total potential is given by

$$\phi = \frac{1}{\beta}(\phi_I + \phi_V) + \phi_M \qquad (11)$$

where ϕ_M is the potential corresponding to U_M; Eq. (4) for ϕ_I is not altered since Eq. (10) satisfies the solid wall boundary condition. Here

$$\beta = 4\pi \frac{U_\infty a}{|\Gamma|}$$

At this point the velocity field corresponding to the potential field of Eq. (11) may be written as

$$u = \frac{1}{\beta}(U_I + U_V) + U_M \qquad (12)$$

and the velocity u has been nondimensionalized on U_∞. It should be noted that a clockwise rotation of the vortex filament when looking from a side view corresponds to a circulation $\Gamma > 0$. To convect the filament the velocity due to the vortex itself, U_V, and its image U_I must be computed. The methods employed to do this are described next.

Vortex Core Flow

The crucial difference between the motion of a two-dimensional, straight vortex filament and a three-dimensional filament is the presence of a local self-induced velocity field that, in general, imparts a finite curvature to the vortex. The velocity field corresponding to a general vortex filament in free space is given by Eq. (9) provided the field point X is not on the vortex filament. However, to advance the filament we must evaluate Eq. (12) on the filament, and for one value of $X = X'$ Eq. (9) becomes unbounded there. This is a reflection of the fact that Eq. (9) is not valid as the core of the filament is approached; Callegari and Ting[21] have suggested that the singularity may be removed by the incorporation of the physical effect of the viscosity in the core, and they show how to match this core flow solution with the inviscid solution for the case of a general, finite length, closed filament in free space. Their work is in the process of being adapted to the present problem; however, the analysis is very complex, and in this work a more conventional approach to remove the singularity in U_V will be adopted.

In the present work we adopt a cutoff procedure due originally to Moore[22] and employed recently in the work of Hon and Walker[2] in their calculations of the flowfield induced by convected hairpin vortices. The method entails inserting a parameter μ into the denominator of Eq. (9) to regularize the integrand when X is on the filament; in this case, Eq. (9) becomes

$$U_V(X, t) = -\text{sgn}(\Gamma) \int_C \frac{(X - X') \times dX'}{(|X - X'|^2 + \mu^2)^{3/2}} \qquad (13)$$

The value of μ is fixed by appeal to the exact solution for the vortex ring problem,[22,23] and the result is

$$\ell_n\left(\frac{\mu^*}{a_v^*}\right) = -\frac{1}{2} - \frac{4\pi^2}{\Gamma^2}\int_0^{a_v^*} v'^2 r^* \, dr^* + \frac{8\pi^2}{\Gamma^2}\int_0^{a_v^*} w'^2 r^* \, dr^* \qquad (14)$$

where v' and w' are the velocities in the core of the vortex, and a_v^* is the dimensional vortex core radius; r^* and μ^* are also dimensional. For the case of $w' = 0$ and v' corresponding to a Rankine vortex

$$v' = \begin{cases} \dfrac{\Gamma}{2\pi}\dfrac{r^*}{a_v^{*2}} & \text{if} \quad r^* \leq a_v^* \\[3mm] \dfrac{\Gamma}{2\pi r^*} & \text{if} \quad r^* \geq a_v^* \end{cases} \qquad (15)$$

then

$$\mu^* = a_v^* e^{-3/4} \qquad (16)$$

Initial calculations of the motion for the vortex have indicated that the effect of axial flow is relatively minor,[24] and thus, in the interest of convenience, we consider only the case where $w' = 0$. The parameter μ in Eq. (13) is dimensionless and is defined by $\mu = \mu^*/a$ where a is the cylindrical airframe radius.

Self-Induced Motion of the Vortex Filament

The present calculation of the self-induced motion of the vortex filament is essentially that due to Hon and Walker,[2] and in what follows we outline their procedure. The evaluation of successive positions of the vortex filament position is a Lagrangian calculation. Let s be a parametric variable such that the space curve defining the centerline of the filament is given by $X = X(s, t)$; then Eq. (13) may be written

$$U_V(s, t) = -\text{sgn}(\Gamma)\int_C \frac{(X - X') \times (\partial X'/\partial s')}{(|X - X'|^2 + \mu^2)^{3/2}} \, ds' \qquad (17)$$

As pointed out by Hon and Walker,[2] μ is often small for small-core vortices, and consequently numerical evaluation of Eq. (17) is still difficult; Hon and Walker,[2] following Moore,[22] suggest using a Taylor series expansion of the integrand about the local filament point. The form of Eq. (17) obtained by Moore using this procedure is

$$U_V(s, t) = \text{sgn}(\Gamma)\int_C \left[\frac{(\partial X'/\partial s') \times (X - X')}{(|X - X'|^2 + \mu^2)^{3/2}} \right.$$

$$\left. -\left(\frac{\partial X}{\partial s} \times \frac{\partial^2 X}{\partial s^2}\right)_s P(s') \right] ds'$$

$$+ \text{sgn}(\Gamma)\left(\frac{\partial X}{\partial s} \times \frac{\partial^2 X}{\partial s^2}\right)_s \int_C P(s') ds' \qquad (18)$$

where

$$P(s') = \frac{\dfrac{1}{2}(s' - s)^2}{[(s' - s)^2 (\partial X/\partial s)_s^2 + \mu^2]^{3/2}} \qquad (19)$$

The second integral in Eq. (18) may be calculated analytically, whereas the first integral can be evaluated numerically using a

standard integration scheme. The accuracy of the numerical calculations of the first integral may be significantly improved if further terms in the Taylor series are included. Hon and Walker[2] suggest that more terms are necessary to compute accurate solutions for filaments with small vortex cores moving near solid boundaries. If $R(s', s)$ denotes the integrand of the first integral in Eq. (18), higher order terms in the Taylor series are given by

$$R(s' - s) = D(s' - s)^3 + E(s' - s)^4 + \ldots$$

for $s' \sim s$, where D and E are complicated vector functions given in Appendix D of Hon and Walker[2] and will not be given here for brevity. Consequently, when the field point approaches a filament point, the integrand of the first integral in Eq. (18) is equal to $R(s', s)$ and the integral around $s = s'$ may be performed analytically; terms through $(s'-s)^4$ are used in the calculations. The evolution of an initially straight vortex filament above a circular cylinder as in Fig. 1 may then be described as follows. The deformation of the vortex filament will be local in character and occurs between, say, $x = -l$ and $+l$ where l is a parameter. Assume that the parametric variable s' ranges from $s' = -\infty$ to $+\infty$. Then the infinite integral in Eq. (18) can be evaluated as follows. The vortex ends from $(-\infty, -l)$ and from (l, ∞) are assumed to be straight, and the associated integrals may be computed analytically. For each value of s on the filament the remaining portion of the vortex filament is broken into three segments: one from $-l$ to $s - \Delta s$, one from $s - \Delta s$ to $s + \Delta s$, and one from $s + \Delta s$ to l. Only those integrals from $-l$ to $-\Delta s$ and Δs to l need to be computed numerically. Here Δs is the spacing between the grid points defining the vortex. The parameter l must be determined by numerical experimentation, and in all cases considered $l = 5$ is sufficient to insure that the straight portions of the filament are not affected by the deformation of the filament near the cylinder. The limits of the integral involving R are somewhat a matter of choice; however, the choice of the interval $(-\Delta s, \Delta s)$ gives excellent results when the numerical mesh on the filament is refined.

Having described the calculation of the self-induced portion of the velocity field, we now discuss the calculation of the image field.

Image-Induced Velocity Field

The solution for the velocity field due to the image of the filament may be obtained by direct differentiation of Eq. (4) with the radial velocity due to a vortex filament in free space at the cylinder boundary given by Eq. (5). Substituting Eq. (5) into Eq. (4) and switching the order of the integral and sum, one can write Eq. (4) as

$$\phi_I = -\frac{\text{sgn}(\Gamma)}{4\pi^2} \sum_{m=-\infty}^{\infty} \int_{-\pi}^{\pi} \int_C (I_1 + I_2)\, ds' \cos\, m(\theta - \alpha)\, d\alpha$$

(20)

where

$$I_1 = 2\int_0^\infty A K_1(c_1 k)\, \frac{K_m(rk)}{K_m'(k)}\cos k(z - z')\, dk$$

$$I_1 = -2\int_0^\infty B K_0(c_1 k)\, \frac{K_m(rk)}{K_m'(k)}\sin\, k(z - z')\, dk$$

The velocity components can be obtained by differentiation under the integral, and it follows that

$$U_{Ir} = -\frac{\text{sgn}(\Gamma)}{4\pi^2} \sum_{m=-\infty}^{\infty} \int_{-\pi}^{\pi} \int_C (I_3 + I_4)\, ds' \cos\, m(\theta - \alpha)\, d\alpha$$

(21)

$$U_{I\theta} = -\frac{\text{sgn}(\Gamma)}{4\pi^2} \sum_{m=-\infty}^{\infty} \int_{-\pi}^{\pi} \int_C \frac{m}{r}(I_5 + I_6)\, ds' \sin\, m(\theta - \alpha)\, d\alpha$$

(22)

$$U_{Iz} = -\frac{\text{sgn}(\Gamma)}{4\pi^2} \sum_{m=-\infty}^{\infty} \int_{-\pi}^{\pi} \int_C (I_7 + I_8)\, ds' \cos\, m(\theta - \alpha)\, d\alpha$$

(23)

where the specific forms of the integrals I_3–I_8 are given in the Appendix; in these equations the subscript I denotes the image. The self-induced velocity field is given in Cartesian coordinates because it is simpler to advance the vortex in Cartesian space. The image velocity field may be rewritten in Cartesian coordinates as

$$U_I = (U_{Ir}\cos\,\theta - U_{I\theta}\sin\,\theta)\,\hat{i} + (U_{Ir}\sin\,\theta + U_{I\theta}\cos\,\theta)\,\hat{j} + U_{Iz}\hat{k}$$

(24)

and this expression will be used to convect the vortex. To evaluate the integrals along the space curve in Eqs. (21–23), we use a procedure similar to the evaluation of the self-induced velocity.

Filament Motion

The velocity field induced by a general vortex filament in the presence of the cylinder and in a mean streaming motion is given by Eq. (12). To calculate the motion of the vortex filament, we evaluate Eq. (12) on the filament; each point is then advanced according to the evolution equation

$$\frac{\partial X}{\partial t}(s, t) = \beta u$$

(25)

where the time scale t is defined by

$$t = \frac{U_\infty}{\beta a}t^*$$

(26)

and t^* is dimensional.

In general, the initial position of the filament is given by

$$X(s, t = 0) = f(s)\hat{i} + y_s\hat{j} + z_s\hat{k}$$

(27)

Here we take $y_s = 2.0$; also, $z_s = 0$ and $f(s) = s$.

Pressure Field

To obtain the surface pressure field, we begin by noting that the pressure gradients on the cylinder are obtained from Euler's equations which are given, in dimensionless form, by

$$\frac{1}{\beta}\frac{\partial u}{\partial t} + (u \cdot \nabla) u = -\nabla p$$

(28)

where $p = (p^* - p_\infty)/\rho U_\infty^2$, where p^* is dimensional and p_∞ is a constant reference pressure. Using the definition of the velocity potential $u = \nabla\phi$, after interchange of time derivative and gradient, we find that

$$\nabla\left(\frac{1}{\beta}\frac{\partial\phi}{\partial t} + \frac{|u|^2}{2} + p\right) = 0$$

(29)

Integrating Eq. (29), we have

$$\frac{1}{\beta}\frac{\partial\phi}{\partial t} + \frac{|u|^2}{2} + p = f_0(t)$$

(30)

where f_0 is the Bernoulli constant obtained by evaluating the left side of Eq. (29) at the beginning of the integration path; if all paths begin at $z = -\infty$ and $\theta = \theta_0$, then $f_0 = \frac{1}{2}U_M^2$ ($r = 1, \theta_0$) where θ_0 is a parameter.

The velocity potential ϕ includes the effect of the mean flow, the image, and the vortex itself. The image potential is given by Eq. (4), and the mean flow potential may be obtained directly by integration of Eq. (10). The potential due to the vortex itself is not easy to obtain, and this is described now. Let X denote a vector coordinate along any path in the fluid; then

$$\phi_V = \phi_V(X_0) + \int_{\text{path}} U_V \cdot dX$$

(31)

where X_0 is the initial point of the curve. Consider the case where the integration path lies on the cylinder surface at a fixed angular location ϕ_0 and in the z direction; then

$$\phi_V(\theta_0, z) = \phi_V(\theta_0, -\infty) + \int_{-\infty}^{z} U_{Vz}(\theta_0, z)\, dz \qquad (32)$$

where U_{Vz} is the velocity due to the vortex filament alone in the z direction and is given by an integral of the form

$$U_{Vz} = \int_C \frac{F_1(\theta_0, s')\, ds'}{[F_2^2(\theta_0, s') + (z - z')^2]^{3/2}} \qquad (33)$$

Substituting Eq. (33) into Eq. (32), switching the order of the integration, and integrating in z yields

$$\phi_V(\theta_0, z) = \phi_V(\theta_0, -\infty) + \int_C \frac{F_1}{F_2^2} \left\{ \frac{z - z'}{[F_2^2 + (z - z')^2]^{1/2}} + 1 \right\} ds' \qquad (34)$$

$$(35)$$

In Eq. (34)

$$F_1 = \frac{\partial x'}{\partial s'}(\sin \theta_0 - y') - \frac{\partial y'}{\partial s'}(\cos \theta_0 - x') \qquad (36)$$

and

$$F_2 = c_1(\theta_0, s') \qquad (37)$$

The integral along the filament in Eq. (34) may be evaluated numerically; θ_0 is a parameter and may thus be varied until ϕ_V at all of the desired azimuthal locations is determined.

Numerical Methods

The Lagrangian calculations for the advance of the vortex filament corresponding to the solution of Eq. (25) subject to the initial condition of Eq. (27) are computed by the fourth-order Runge-Kutta method. The vortex is discretized using a mesh size Δs, and the filament grid points are given parametrically by

$$s_j = (j - M/2 - 1)\Delta s \qquad (38)$$

where $M = 100$, $j = 1, \ldots, M + 1$, and $\Delta s = 0.1$; the length $2l$ over which the filament may deform is thus 10. Solutions have been computed for several larger values of l corresponding to $2l = 12$ and 16 with no change in the computed solution to three digits. Use of the preceding numerical parameters to define the filament and of the time step $\Delta t = 0.01$ insures at least three-figure accuracy in the computed vortex trajectory as those parameters are reduced.

The self-induced velocity of the filament is given by Eq. (18). Simpson's rule[25] has been employed for that integral. The derivatives with respect to s, say $\partial X/\partial s$, have been computed using the second-order central difference scheme according to

$$\left. \frac{dX}{ds} \right|_{s = sj} = \frac{X_{j+1} - X_{j-1}}{2\Delta s} + \theta(\Delta s^2) \qquad (39)$$

There are a number of other numerical parameters in the present calculations, and a series of numerical tests were carried out to insure the accuracy of the computations. First, for the computations of the vortex trajectory, the real valued integrals corresponding to the calculation of the image-induced velocities are all of the Fourier type in k. A transformation in k is employed to cluster the grid near $k = 0$, and the resulting integrals are computed using Simpson's rule. A total of 100 points in k are used to insure three-digit accuracy compared with the solution for 200 points when the distance between the vortex and the cylinder is no less than two core radii.

The integrals in the angular variable α [see Eqs. (21–23)] are calculated using a uniform mesh. A grid size $\Delta\alpha = 2\pi/40$ is employed to insure three-digit accuracy at all times compared with the solutions for $\Delta\alpha = 2\pi/80$. In addition, the number of modes in the azimuthal direction must be specified; here again, several values were tried corresponding to 8, 10, and 12 modes with no difference in the computed solution for the filament position to three digits.

Second, the computations of the image-induced velocities at the surface of the cylinder used in the evaluation of the surface pressure field are performed using a different procedure. Because the airframe surface is fixed and a computational grid is easily defined, it is more efficient computationally to use the fast Fourier transform (FFT) technique to obtain the surface pressure. The Fourier transform of any flow quantity is defined as

$$\hat{G}(m, k) = \int_{-\infty}^{\infty} \int_{-\pi}^{\pi} G(\theta, z) \exp(-im\theta - ikz)\, d\theta\, dz \qquad (40)$$

where $m = 0, \pm 1, \pm 2, \pm 3, \ldots$, is the transform variable corresponding to θ, and k (real) is the transform variable corresponding to z. A finite range $-L \leq z \leq L$ is used in the numerical scheme to represent the infinite range of z. An adequate range of z is determined by comparing the results with the results of larger ranges. Several tests have been conducted to determine the appropriate range, and the value $L = 12.8$ is used here. In addition, values of $\Delta z = 0.05$, 0.1, and 0.2 were tested with at least two-digit agreement between all three grid sizes; however, to obtain better, more resolved results for the pressure, especially in the latter stages of the calculations, the present results are for $\Delta z = 0.05$ with the number of points $M_z = 512$. The number of points in the θ direction is taken to be $M_\theta = 32$, which insures at least three-digit accuracy compared with $M_\theta = 64$. The discretization of the Fourier transform is carried out as follows:

$$-\pi \leq \theta \leq \pi, \quad \theta_i = (i - 1 - M_\theta/2)\Delta\theta \text{ for } i = 1, 2, \ldots, M_\theta \qquad (41)$$

$$-L \leq z \leq L, \quad z_j = (j - 1 - M_z/2)\Delta z \text{ for } j = 1, 2, \ldots, M_z \qquad (42)$$

$$-\bar{L} \leq k \leq \bar{L}, \quad k_n = (n - 1 - M_z/2)\Delta k \text{ for } n = 1, 2, \ldots, M_z \qquad (43)$$

where the grid spacings $\Delta\theta$, Δz, and Δk should satisfy the following relations:

$$\Delta\theta = \frac{2\pi}{M_\theta}, \qquad \Delta z = \frac{2L}{M_z}, \qquad \Delta k = \frac{\pi}{L} \qquad (44)$$

and M_z and M_θ are chosen to be power of 2 to use the fast Fourier transform efficiently.

For brevity, we only outline the procedure to obtain, for example, $U_{Iz}|_{r=1}$. First, the velocity $U_{Vr}|_{r=1}$ is computed using Eq. (9). Then its forward transform $(\partial\hat{\phi}_V/\partial r)|_{r=1}$ appearing in Eq. (4) is obtained from Eq. (2) using the FFT. The Fourier transform of $\hat{\phi}_I|_{r=1}$ is then computed using the integrand in Eq. (4) that is given by

$$\hat{\phi}_I|_{r=1} = \left. \frac{\partial\hat{\phi}_V}{\partial r}\right|_{r=1} \times \frac{K_m(|k|)}{|k|\, K_m'(|k|)} \qquad (45)$$

To obtain $U_{Iz}|_{r=1}$, which is equal to $(\partial\theta_I/\partial z)|_{r=1}$, we invert the quantity $ik\hat{\phi}_I|_{r=1}$ back to the physical domain using the inverse Fourier transform. All other image-induced velocity components on the surface of the cylinder are obtained in a similar way.

Last, because the velocities are more sensitive to numerical error than are the filament positions, it has been found necessary to use a much finer grid over the vortex filament in calculating the surface pressure; thus $\Delta s = 0.025$ in evaluating the Biot-Savart
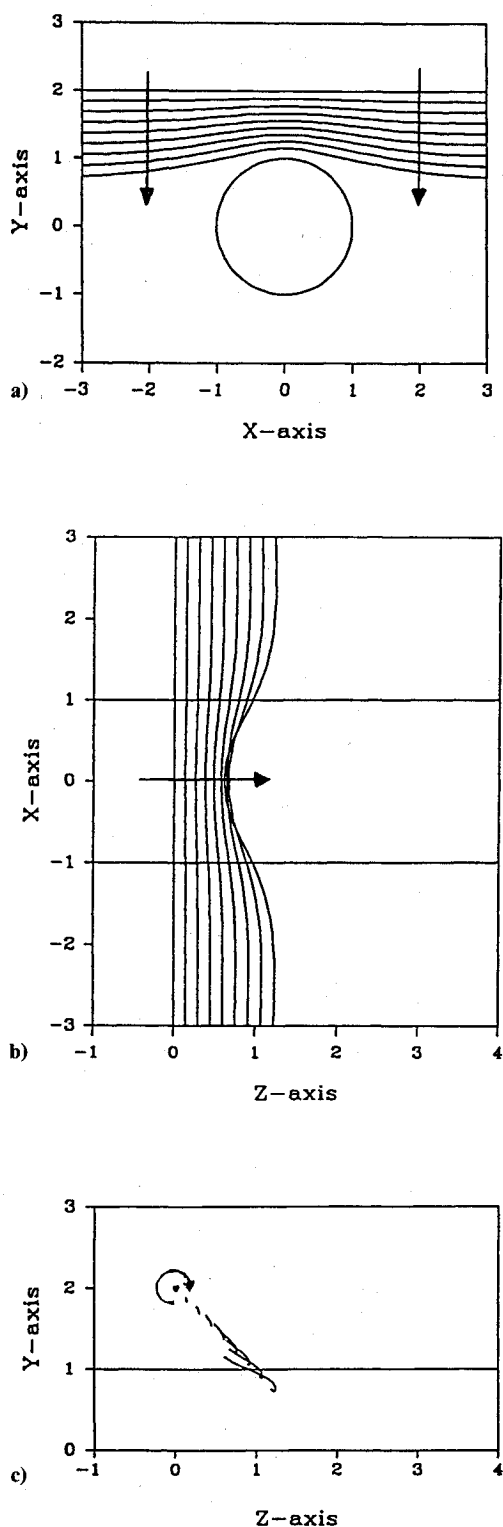
for the filament position for $\alpha = 1$, and $\beta = 3$ for the case where the core size is fixed at $a_v = 0.1$; this results in a value of $\mu = 0.047$, which is characteristic of core sizes in experiments. The sign of the circulation is positive and is also shown and corresponds to the experimental situation of Liou et al.[11] (see also Refs. 12 and 13). Note the bending of the vortex filament as it approaches the airframe; in this figure, the calculation was stopped after 40 time steps, and thus the total time of the calculation is $t = 0.4$; at the last time shown, the head of the vortex is just over one core radius from the cylinder. Soon after this time a kink begins to appear in the vortex at the midpoint $s = 0$ and the calculation fails. Similar results are obtained for the case of $\alpha = 2$ and they are shown in Fig. 3; here the convection distance in the z direction is larger because
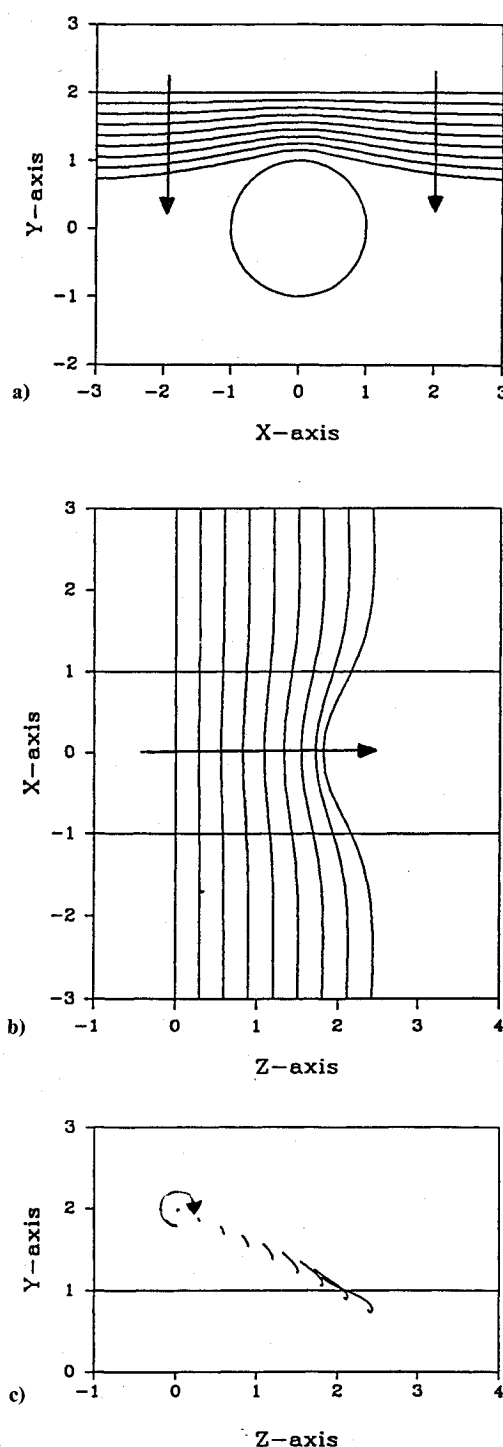

Fig. 2   Vortex positions for the case where $\alpha = 1.0$ and $\beta = 3.0$: a) end view, b) top view, and c) side view. Here $\Delta t = 0.01$ and the vortex core radius $a_v = 0.1$. Arrow denotes increasing time.

integral [see Eq. (9)] in all of the pressure and pressure gradient calculations presented.

Results

There are three main parameters whose effect is of interest here; these are α, β, and the assumed dimensionless vortex core size a_v. In all of the following cases, the initial configuration of the vortex filament is $x = s$, $y = 2.0$, and $z = 0$, and the results are plotted every five time steps beginning at time step 1. Figure 2 shows the results
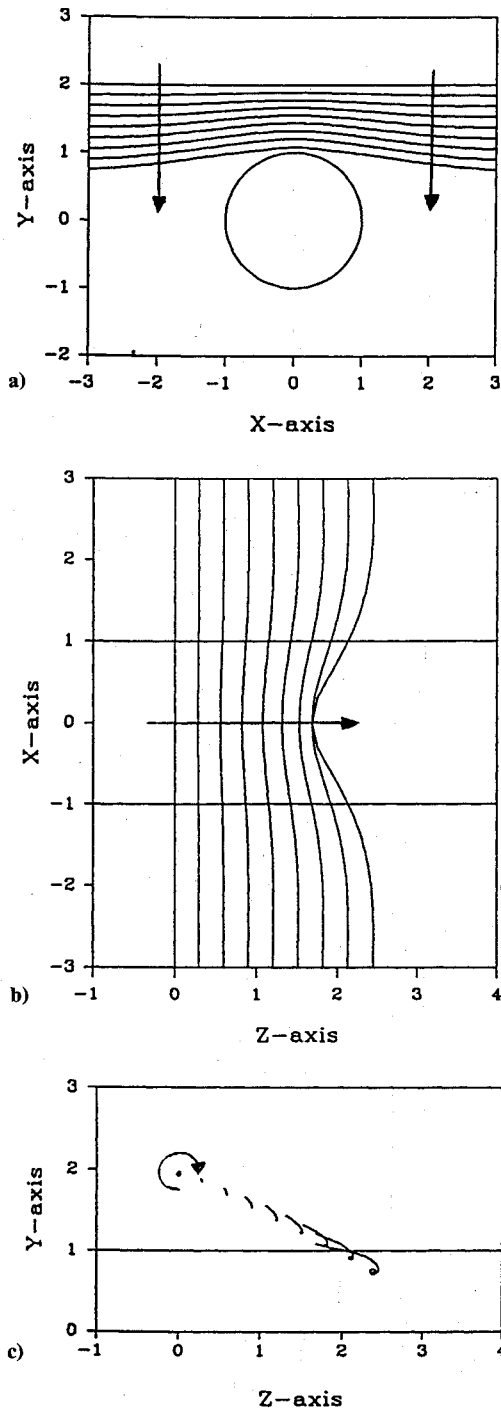

Fig. 3   Vortex positions for the case where $\alpha = 2.0$ and $\beta = 3.0$: a) end view, b) top view, and c) side view. Here $\Delta t = 0.01$, and the vortex core radius $a_v = 0.1$. Arrow denotes increasing time.

the mean axial flow is larger; the qualitative characteristics of this case are similar to those of Fig. 2. The effect of vortex core size is depicted in Fig. 4 for the case of $\alpha = 2$ and $\beta = 3$. Here $a_v = 0.05$, and note that the results are very similar to the preceding results except in the latter few time steps; in particular the vortex head moves faster toward the cylinder with a slower speed in the z direction, a situation not evident in the larger core result (Fig. 3); similar results are noted for the $\alpha = 1$ case. At the last time step shown for $a_v = 0.05$, the head of the vortex is just over one core radius from the cylinder, and again the total dimensionless time of the calculation is $t = 0.4$.

For all of the results shown so far, the sign of the circulation has been assumed to be positive; the experimental situation described

Fig. 4 Vortex positions for the case where $\alpha = 2.0$ and $\beta = 3.0$: a) end view, b) top view, and c) side view. Here $\Delta t = 0.01$, and the vortex core radius $a_v = 0.05$. Arrow denotes increasing time.
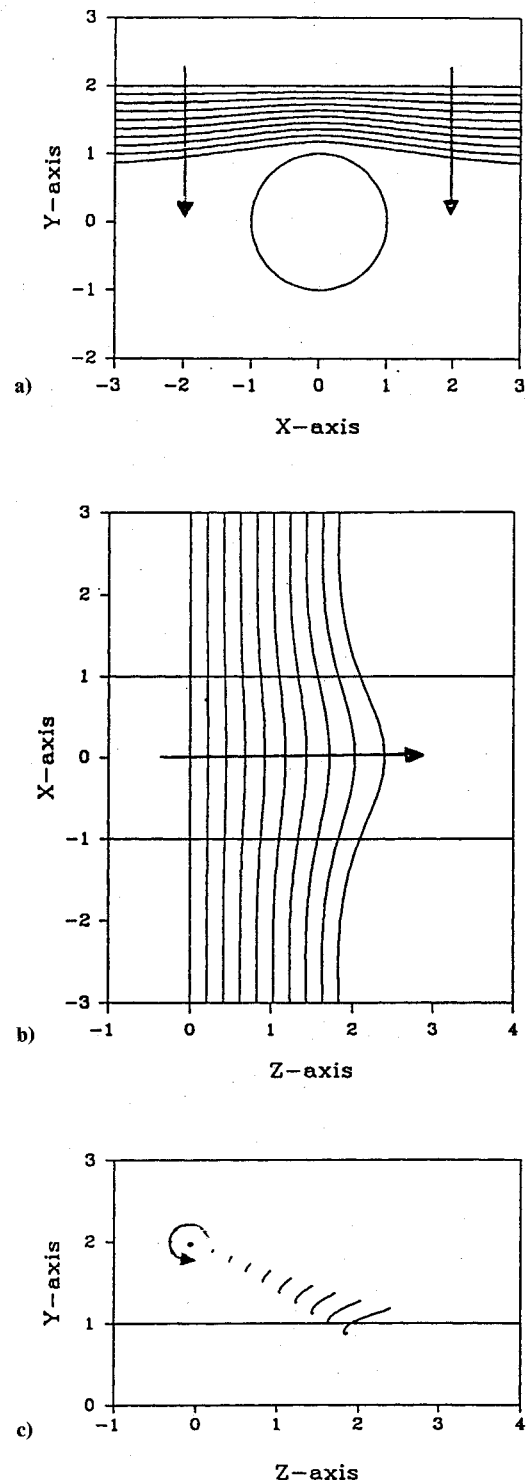
Fig. 5 Vortex positions for the case of Bi and Leischman where $\alpha = 1.72$ and $\beta = 2.4$: a) end view, b) top view, and c) side view. Here sgn(Γ) $= -1$, $\Delta t = 0.01$, and the vortex core radius $a_v = 0.1$. Arrow denotes increasing time.

by Bi and Leishman[14,15] and Leishman and Bi[16] may be modeled to a first approximation by merely switching the sign of the circulation. The experimental conditions correspond to $\alpha = 1.72$ and $\beta = 2.4$; the core size has been fixed at 0.1. Figure 5 shows the results for an advance ratio of 0.075. The end view of the vortex motion is similar to the preceding results; however, the other two views are substantially different. Note in particular the side view where the trajectory suggests a grazing type of motion rather than a direct collision. We note here, however, that because of the presence of
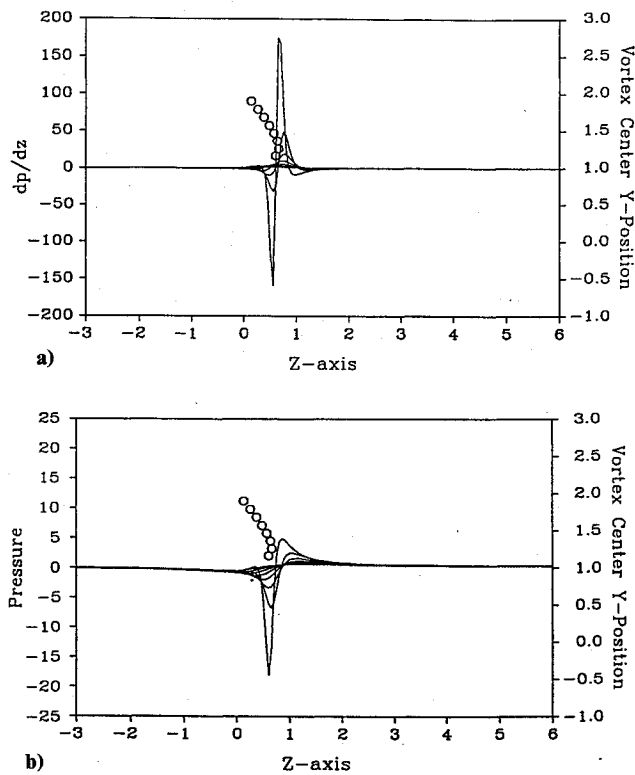
Fig. 6 Results for the axial pressure gradient and pressure for the parameters of Fig. 2: a) pressure gradient and b) pressure. The circles denote the positions of the vortex center.
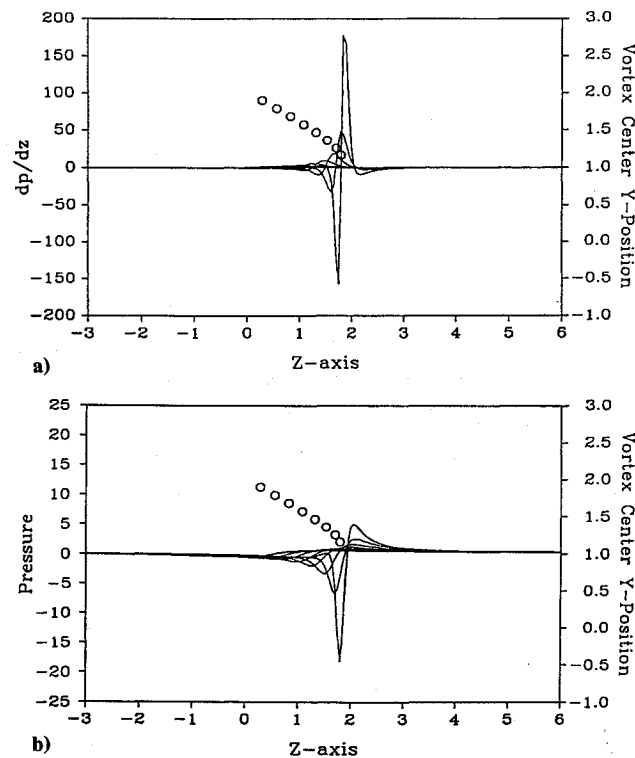

Fig. 7 Results for the axial pressure gradient and pressure for the parameters of Fig. 3: a) pressure gradients and b) pressure. The circles denote the positions of the vortex center.

the downwash, the vortex head will eventually collide with the airframe, although at a substantially different angle than is the case for positive circulation. It should be noted that the initial position of the vortex does not necessarily correspond to that of the experiments of Bi and Leishman[15]; moreover, the vortex core radius has been fixed as noted earlier. Consequently, quantitative comparison

of the present results with the data of Bi and Leishman[14,15] must await future work. However, it is believed that the essential features of the vortex motion may be captured using the present model.

The rather mild filament curvature induced by the cylinder belies the striking nature of the pressure field under the vortex. In all subsequent results, the axial pressure gradient on the air-
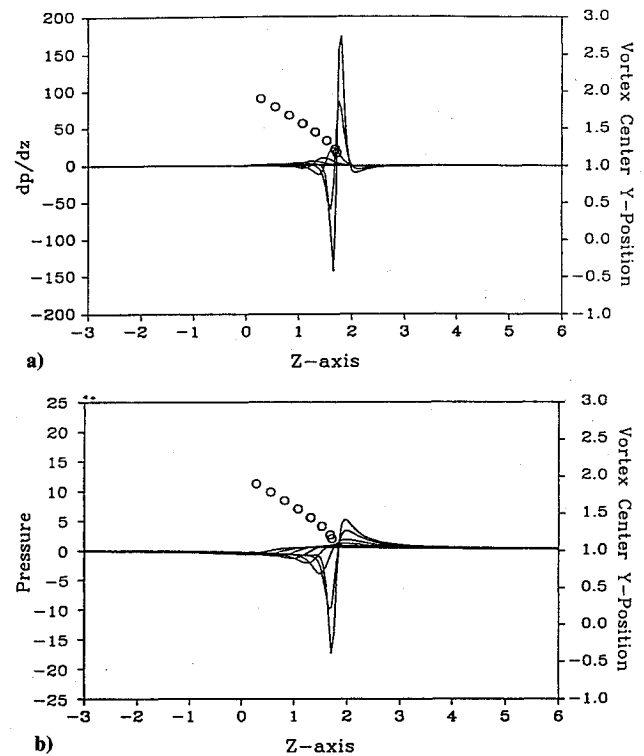

Fig. 8 Results for the axial pressure gradient and pressure for the parameters of Fig. 4: a) pressure gradient and b) pressure. The circles denote the positions of the vortex center.
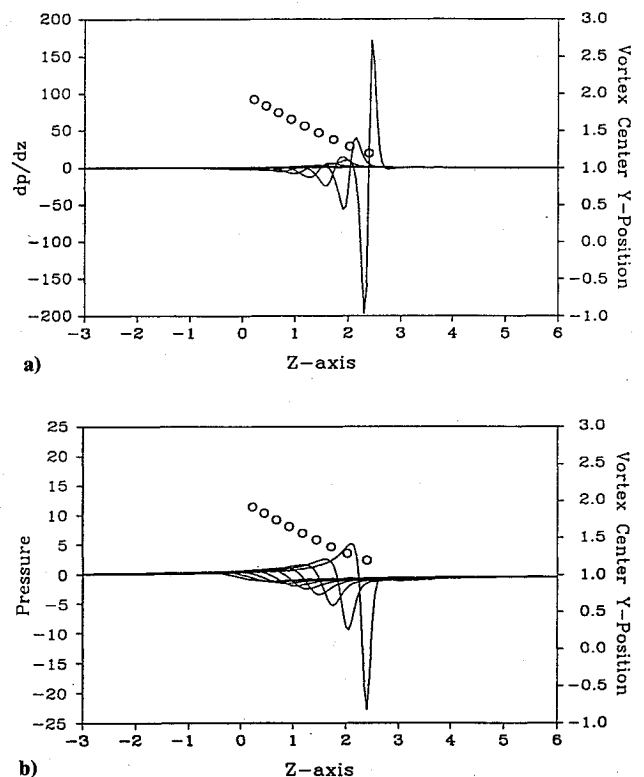

Fig. 9 Results for the axial pressure gradient and pressure for the parameters of Fig. 5: a) pressure gradient and b) pressure. The circles denote the positions of the vortex center.

frame $\partial p/\partial z$ is plotted at $\theta_0 = \pi/2$ at the time steps corresponding to those plotted for the vortex positions; however, the initial pressure gradient and pressure are not plotted. Figure 6 shows the results for the pressure gradient and pressure for the parameters of Fig. 2. Also shown is the relative position of the vortex head. Note the emergence of a large adverse pressure gradient just downstream of the head of the vortex. The adverse pressure gradient causes a large suction peak at the axial location of the head of the vortex. Similar results are observed for $\alpha = 2$ and $\beta = 3$ in Fig. 7; the difference in the pressure results at the earlier times is due to the difference in the vortex position. However, the magnitude of the maximum suction peak is nearly equal in both cases; this is believed to be due to the fact that the local vortex y position near the pressure evaluation point is very similar in each case. In Fig. 8, the core size $a_v = 0.05$ and all other parameters are as in Fig. 7; here the results are plotted every five time steps beginning at $t = 0.05$. The last time step shown in Fig. 8 corresponds to $t = 0.37$, and at this time the vortex head position is at nearly the same y position as that for the parameters of Fig. 7 at $t = 0.4$. Consequently, the maximum suction peak in each case is nearly equal, although the time evolution of the peak is substantially different. This can be seen by noting that in the early stages of the calculation, when the vortex is many core radii from the cylinder, the pressure traces in each case are nearly the same; after $t = 0.3$, as the vortex approaches the cylinder, the two solutions begin to deviate.

Figure 9 shows results for negative circulation corresponding to the filament evolution depicted in Fig. 5. Note that the character of the solution for both the pressure and the pressure gradient is much different than for the case of positive circulation described in the preceding results. The magnitude of the adverse pressure gradient and the pressure should be compared with Figs. 6–8; in each case the negative circulation yields much bigger values in the latter stages of the calculation. This appears to be due to the fact that the negative value of the circulation induces a larger total axial velocity on the airframe than is the case with the positive value of the circulation. It should be noted here that, in the work of Bi and Leishman,[15] the results for the pressure distribution are plotted as a function of time at fixed locations on the airframe; in the present case the results have been plotted at a number of locations on the airframe for several times. The precise details of the pressure field in the work of Bi and Leishman[15] depend on the relative position of the pressure sensors on the airframe, and several different types of pressure traces have been identified. In particular, the form of presentation of Bi and Leishman[15] may be obtained by fixing attention on a specific point on the airframe and observing the behavior of the pressure at successive times. The present results appear to be consistent with those of Bi and Leishman[15] during the period before vortex-airframe collision in that they indicate a rapid drop in pressure with time as the vortex approaches. The magnitude of the drop is dependent on the relative position of the sensor point and the position of vortex impact as discussed in Ref. 15.

Vortex Structure

As mentioned, the value of μ in Eq. (13) is obtained assuming that the vortex core structure is locally axisymmetric. To investigate the possible modification of this structure as the filament approaches the cylinder, the velocity field around the core has been investigated. The velocity field relative to the vortex filament at $s = 0$ has been calculated at $\bar{r} = a_v$ where $\bar{r}$ denotes a local coordinate system attached to the filament. These results are shown in Fig. 10 for the case of $\alpha = 2$ and $\beta = 3$; the vortex core size has been fixed at 0.1. In this section the variable θ refers to the local angular coordinate relative to the vortex core as depicted in Fig. 10. The results are shown at $t = 0$, indicated by the straight lines, and at the later times in the calculations when $t = 0.35, 0.36, 0.37, 0.38, 0.39$ and 0.4. Note that for much of the time the azimuthal velocity (relative to the filament) is constant at just over -6; however, very late in the calculation, some azimuthal variation begins to emerge. This coincides with the development of a finite radial velocity at this location. A rapid increase in the magnitude of the azimuthal velocity occurs around $\theta = 270$ deg, which coincides
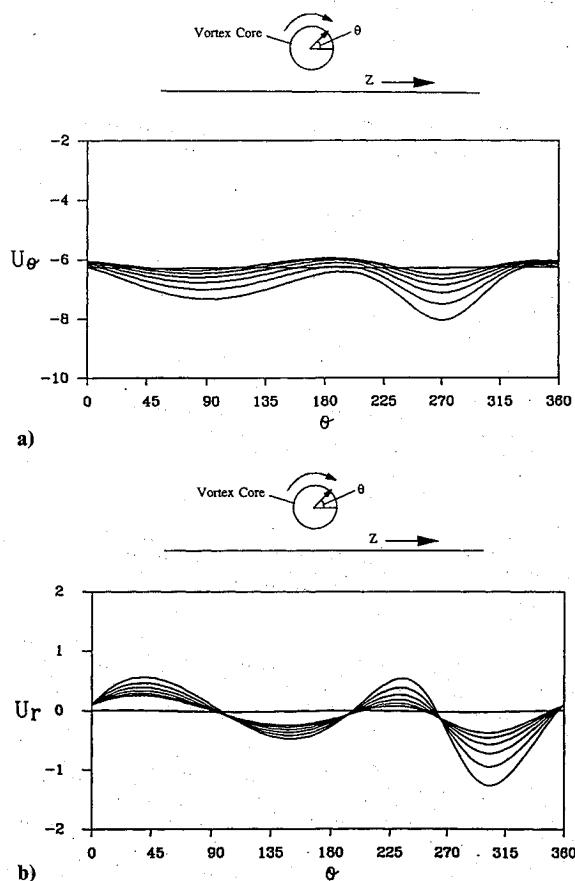

Fig. 10 Azimuthal and radial velocity relative to the vortex core at the assumed vortex core radius $\bar{r} = a_v$ around the vortex as a function of local polar angle. The curves are plotted at $t = 0$ (straight line) and at later times, $t = 0.35, 0.36, 0.37, 0.38, 0.39$, and 0.4. These results are for $s = 0$. Here $\alpha = 2$, $\beta = 3$, and $a_v = 0.1$.

with the portion of the vortex nearest the cylinder. In the work of Callegari and Ting,[21] the image-induced component of the local velocity field around the vortex is zero; and the azimuthal velocity just outside the vortex is the free vortex axisymmetric solution; therefore the core flow will remain axisymmetric if it had originally been axisymmetric. Investigation of the local velocity field at points removed from $s = 0$, namely, at $s = 1$ and 4, reveals that the flow is indeed nearly axisymmetric at the vortex boundary for all times. It should be mentioned that the azimuthal direction with respect to the core of the vortex at $\theta = 270$ deg corresponds to the axial flow (z direction) with respect to the cylinder.

The genesis of the deformation of the vortex core may lie in the breakdown of local vortex core symmetry alluded to earlier. As the vortex approaches the cylinder, the image-induced velocity gets progressively larger until it influences the azimuthal velocity field in the vortex core; since the image-induced azimuthal velocity is not axisymmetric with respect to the vortex core, the velocity within the core of the vortex must deviate from the simple Rankine vortex model assumed. This loss of symmetry will result, by local continuity, in the emergence of finite radial and axial velocities within the vortex core (if such an axial velocity did not exist before the strong interaction); the numerical results suggest that this process begins when the vortex is still outside the boundary layer. As Fig. 10 (and the other calculations at $s = 1$ and 4, which are not shown), indicates, this process occurs locally around the points of the filament that are close enough to the cylinder.

Finally, it should be noted that the striking emergence of the strong adverse axial pressure gradient spike (Figs. 8–10) is characteristic of many flows generated by vortex motions in two dimensions[26,27] and is expected to play a crucial role in the subsequent local destruction of the vortex and in the development of the boundary layer on the airframe.

Summary and Conclusions

In the present work the motion of a generalized vortex filament outside a circular cylinder has been investigated. We have considered the effect of mean flow, vortex core size, and the relative magnitude of mean downwash and mean axial flow on the evolution of the vortex. It has been shown that the effect of core size is relatively minor until late in the calculation when the vortex core passes within several core radii of the cylinder surface; some variation in the trajectory of the vortex and in the pressure field on the cylinder then occur. The presence of the mean flow in the calculation hastens the interaction of the vortex with the cylinder as expected; the relative importance of the mean downwash and the axial flow also has the expected result; the vortex reaches the cylinder in a shorter axial distance than for the case of smaller α. In particular, three major conclusions may be drawn from these calculations. First, the motion of the vortex induces a very strong axial adverse pressure gradient on the cylinder under the vortex, which results in a very strong negative pressure spike; this negative pressure spike has also been observed in recent experimental work.[11-13] Second, the curvature of the vortex filament appears to remain finite as the filament approaches the cylinder and no kinks arise in the filament profile. This result is also consistent with experimental results[11-13] and suggests that rapid changes in the filament profile are not responsible for the subsequent changes in the vortex structure as it approaches the cylinder. Third, the present numerical results suggest that the vortex core flow will deviate substantially from the axisymmetric solution assumed as the vortex approaches the airframe. This may be the physical mechanism for the large flattening of the vortex core flow seen in certain experiments.[10,11] The effect of core size is limited to the latter stages of the calculations when the vortex approaches within a few core radii of the airframe.

It is useful to discuss the effect of viscosity on the vortex as it approaches very close to the airframe. For all of the calculations presented here, the vortex core is nominally outside the boundary layer, and so the flow outside the core is still inviscid. At the present time we are investigating the nature of the viscous flow on the airframe under the vortex as it approaches[28,29]; the results indicate the appearance of a reversed flow region that eventually is likely to be ejected into the main stream to interact with the colliding tip vortex. This phenomenon is very difficult to capture numerically, and at the present time only the initial stages of the response of the viscous flow under the vortex have been computed. The actual collision process is a matter for ongoing study.

Appendix

The integrals I_3–I_8 are defined by

$$I_3 = 2 \int_0^\infty AkK_1(c_1 k) \frac{K_m'(kr)}{K_m'(k)} \cos k(z - z') \, dk$$

$$I_4 = -2 \int_0^\infty BkK_0(c_1 k) \frac{K_m'(kr)}{K_m'(k)} \sin k(z - z') \, dk$$

$$I_5 = -2 \int_0^\infty AK_1(c_1 k) \frac{K_m(kr)}{K_m'(k)} \cos k(z - z') \, dk$$

$$I_6 = 2 \int_0^\infty BK_0(c_1 k) \frac{K_m(kr)}{K_m'(k)} \sin k(z - z') \, dk$$

$$I_7 = -2 \int_0^\infty AkK_1(c_1 k) \frac{K_m(kr)}{K_m'(k)} \sin k(z - z') \, dk$$

$$I_8 = -2 \int_0^\infty BkK_0(c_1 k) \frac{K_m(kr)}{K_m'(k)} \cos k(z - z') \, dk$$

References

[1]Sheridan, P. F., and Smith, R. F., "Interactional Aerodynamics — A New Challenge to Helicopter Technology," *Journal of the American Helicopter Society*, Vol. 25, No. 1, 1980, pp. 3–21.

[2]Hon, L., and Walker, J. D. A., "An Analysis of the Motion and Effects of Hairpin Vortices," Dept. of Mechanical Engineering and Mechanics, Lehigh Univ., Rept. FM-11, Bethlehem, PA, 1987.

[3]Sarpkaya, T., "Computational Methods with Vortices — The 1988 Freeman Scholar Lecture," *Journal of Fluids Engineering*, Vol. 111, No. 3, 1989, pp. 5–52.

[4]Lewis, T. C., "On the Images of Vortices in a Spherical Vessel," *Quarterly Journal of Pure and Applied Mathematics*, Vol. 16, 1879, pp. 338–347.

[5]Larmor, J., "Electromagnetic and Other Images in Spheres and Planes," *Quarterly Journal of Pure and Applied Mathematics*, Vol. 23, 1889, pp. 94–101.

[6]Lighthill, M. J., "The Image System of a Vortex Element in a Rigid Sphere," *Proceedings of the Cambridge Philosophical Society*, Vol. 52, 1940, pp. 317–321.

[7]Dhanak, M. R., "Interaction Between a Vortex Filament and an Approaching Rigid Sphere," *Journal of Fluid Mechanics*, Vol. 109, 1981, pp. 129–147.

[8]Quakenbush, T. R., and Bliss, D. B., "Vortex Methods for the Computational Analysis of Rotor/Body Interaction," *Proceedings of the 48th Annual Forum of the American Helicopter Society* (Washington, DC), American Helicopter Society, Alexandria, VA, 1992, pp. 475–488.

[9]Komerath, N. M., Mavris, D. M., and Liou, S.-G., "Prediction of Unsteady Pressure and Velocity over a Rotorcraft in Forward Flight," *Journal of Aircraft*, Vol. 28, No. 8, 1991, pp. 509–516.

[10]Simons, I. A., Pacifico, R. R., and Jones, J. P., "The Movement, Structure, and Breakdown of Trailing Vortices from a Rotor Blade," *Proceedings of the CAL/USAA AVLABS Symposium* (Buffalo, NY), 1966.

[11]Liou, S. G., Komerath, N. M., and McMahon, H. M., "Measurement of the Interaction Between a Rotor Tip Vortex and a Cylinder," *AIAA Journal*, Vol. 28, No. 6, 1990, pp. 975–981.

[12]Brand, A. G., McMahon, H. M., and Komerath, N. M., "Surface Pressure Measurements on a Body Subject to Vortex Wake Interaction," *AIAA Journal*, Vol. 27, No. 5, 1989, pp. 569–574.

[13]Brand, A. G., "An Experimental Investigation of the Interaction Between a Model Rotor and Airframe in Forward Flight," Ph.D. Thesis, Georgia Inst. of Technology, Atlanta, GA, 1989.

[14]Bi, N.-P., and Leishman, J. G., "Experimental Study of Rotor/Body Aerodynamic Interactions," *Journal of Aircraft*, Vol. 27, No. 9, 1990, pp. 779–788.

[15]Bi, N.-P., and Leishman, J. G., "Analysis of Unsteady Pressures Induced on a Body in the Vicinity of a Rotor," *Proceedings of the International Specialists' Meeting on Rotorcraft Basic Research*, Georgia Inst. of Technology, Atlanta, GA, 1991, pp. 38-1–38-20.

[16]Leishman, J. G., and Bi, N.-P., "Aerodynamic Interactions Between a Rotor and a Fuselage in Forward Flight," *Journal of the American Helicopter Society*, Vol. 35, 1990, pp. 22–31.

[17]Affes, H., Conlisk, A. T., Kim, J. M., and Komerath, N. M., "Model for Rotor Tip Vortex-Airframe, Part 2: Comparison with Experiment," *AIAA Journal*, Vol. 31, No. 12, 1993, pp. 2274–2282; also AIAA Paper 92-0319, 1992.

[18]Churchill, R. V., *Operational Mathematics*, 3rd ed., McGraw-Hill, New York, 1972, pp. 379, 471.

[19]Affes, H., "Tip-Vortex-Airframe Interactions," Ph.D. Dissertation, Ohio State Univ., Columbus, OH, 1992.

[20]Batchelor, G. K., *Introduction to Fluid Dynamics*, Cambridge Univ. Press, Cambridge, England, UK, 1967, p. 93.

[21]Callegari, A. J., and Ting, L., "Motion of a Curved Vortex Filament with Decaying Vortical Core and Axial Velocity," *SIAM Journal of Applied Mathematics*, Vol. 35, No. 1, 1978, pp. 148–174.

[22]Moore, D. W., "Finite Amplitude Waves on Aircraft Trailing Vortices," *Aeronautical Quarterly*, Vol. 23, Pt. 4, 1972, pp. 307–314.

[23]Ersoy, S., and Walker, J. D. A., "The Viscous Flow Near a Wall by Counter-Rotating Vortex Pairs and Vortex Loops," Dept. of Mechanical Engineering and Mechanics, Lehigh Univ., Rept. FM-8, Bethlehem, PA, 1985.

[24]Affes, H., and Conlisk, A. T., "The Unsteady Interaction of a Three-Dimensional Vortex Filament with a Cylinder," *Proceedings of the International Specialists' Meeting on Rotorcraft Basic Research*, Georgia Inst. of Technology, Atlanta, GA, 1991, pp. 37-1–37-11.

[25]Abramowitz, M., and Stegun, I., *Handbook of Mathematical Functions*, Dover, New York, 1965, p. 886.

[26]Conlisk, A. T., "The Pressure Field in Intense Vortex-Boundary Interaction," AIAA 27th Aerospace Sciences Meeting, AIAA Paper 89-0293, Reno, NV, Jan. 1989.

[27]Peridier, V., Smith, F. T., and Walker, J. D. A., "Vortex-Induced Boundary-Layer Separation, Part 2: Unsteady Interacting Boundary-Layer Theory," *Journal of Fluid Mechanics*, Vol. 232, 1991, pp. 133–165.

[28]Affes, H., and Conlisk, A. T., "The Three-Dimensional Boundary-Layer Flow Due to a Vortex Filament Outside a Circular Cylinder," AIAA 31st Aerospace Sciences Meeting, AIAA Paper 93-0212, Reno, NV, Jan. 1993.

[29]Affes, H., Xiao, Z., Conlisk, A. T., Kim, J. M., and Komerath, N. M., "The Three-Dimensional Boundary Layer Flow Due to a Rotor Tip Vortex," AIAA 24th Fluid Dynamics Conference, AIAA Paper 93-3081, Orlando, FL, July 1993.